

Article

Study on the Hydrodynamic Performance of the Beam Used in the Antarctic Krill Beam Trawl

Yuyan Li ¹, Zheng Liu ², Zhongqiu Wang ¹ , Xun Zhang ¹, Lumin Wang ¹, Yu Zhang ¹, Shuo Ma ¹, Guangrui Qi ¹ and Yongjin Wang ^{1,*}

¹ East China Sea Fisheries Research Institute, Chinese Academy of Fishery Sciences, Shanghai 200090, China; liyuyan@ecsf.ac.cn (Y.L.); wangzq@ecsf.ac.cn (Z.W.); zhangx@ecsf.ac.cn (X.Z.); lmwang@ecsf.ac.cn (L.W.); zhangy@ecsf.ac.cn (Y.Z.); mashuo_ecsf@126.com (S.M.); qigr@ecsf.ac.cn (G.Q.)

² CNFC Overseas Fisheries Co., Ltd., Beijing 100031, China; liuzheng@cofc.com.cn

* Correspondence: wangyj@ecsf.ac.cn; Tel.: +86-2165680276

Abstract: The beam trawl is one of the primary operational trawls for Antarctic krill, and its beam provides horizontal expansion support for the trawl net. The hydrodynamic performance of the beam significantly affects the vertical expansion and sinking performance of the trawl, as well as impacts the energy consumption of the fishing vessel. In this study, the beam of the Antarctic krill trawl used on the “Shen Lan” fishing vessel served as a prototype. Three types of beams, cylindrical, airfoil, and elliptical, were designed. The hydrodynamic performances of beams with different shapes at different angles of attack were studied using numerical simulation, and the accuracy of the numerical simulation was validated through the flume test. The results show that the cylindrical beam has a higher drag coefficient and a lower lift coefficient, compared to the airfoil beam and the elliptical beam. Under different angles of attack, the cylindrical beam’s drag coefficient is, on average, 49.54% higher than that of the airfoil beam and 59.74% higher than that of the elliptical beam. Its lift coefficient is 87.79% lower than that of the airfoil beam and 85.06% lower than that of the elliptical beam, respectively. At different angles of attack, the hydrodynamic coefficients of the airfoil beam and the elliptical beam are similar, and their trends, with respect to the angle of attack, are generally consistent. The drag coefficients increase with an increasing angle of attack, while the lift coefficients show a trend of initially increasing and then decreasing with an increasing angle of attack. The absolute values of the lift coefficients for the airfoil beam and the elliptical beam both reach their maximum values at an angle of attack of 45°, with values of 0.703 and 0.473, respectively. Compared to the cylindrical beam, the hydrodynamic performances of the airfoil beam and elliptical beam are superior.

Keywords: trawl beam; Antarctic krill trawl; hydrodynamic performance; flume test; numerical simulation

Key Contribution: The present work investigated the hydrodynamic performances of beams used in Antarctic krill trawls and conducted a comparative analysis of the hydrodynamic characteristics of beams with varying shapes for the first time. The critical angles of attack for airfoil and elliptical beams were obtained. The shape had a significant influence on the hydrodynamic performances of beams.



Citation: Li, Y.; Liu, Z.; Wang, Z.; Zhang, X.; Wang, L.; Zhang, Y.; Ma, S.; Qi, G.; Wang, Y. Study on the Hydrodynamic Performance of the Beam Used in the Antarctic Krill Beam Trawl. *Fishes* **2024**, *9*, 17. <https://doi.org/10.3390/fishes9010017>

Academic Editor: Xinjun Chen

Received: 30 September 2023

Revised: 17 December 2023

Accepted: 28 December 2023

Published: 29 December 2023



Copyright: © 2023 by the authors. Licensee MDPI, Basel, Switzerland. This article is an open access article distributed under the terms and conditions of the Creative Commons Attribution (CC BY) license (<https://creativecommons.org/licenses/by/4.0/>).

1. Introduction

Antarctic krill (*Euphausia superba*) plays a pivotal role as a “keystone species” within the Antarctic ecosystem, and it stands out as one of the largest single-species harvestable resources found in the ocean [1,2]. With its rich protein content and valuable unsaturated fats, it holds considerable nutritional significance and offers tremendous potential for commercial exploitation [3]. Its commercial development has garnered much attention

from various countries, given its substantial economic value and extensive prospects for growth [4].

Commercial harvesting of Antarctic krill began in the 1970s and was initially conducted primarily by the former Soviet Union, Japan, and South Korea. In recent years, Norway and China have seen a gradual increase in their krill catch [5]. Since 2010, Norway has been the leading nation in Antarctic krill fishing. In 2014, Norwegian catches of Antarctic krill accounted for approximately 58% of the total landed krill, followed by South Korea and China [5].

The Antarctic krill is a smaller mesopelagic species with a lower swimming speed [6]; therefore, the midwater trawl is the primary fishing gear used for catching this species. Many scholars have conducted research on the design and optimization of the midwater trawl for Antarctic krill. For example, Wan et al. [2] designed a large Antarctic krill trawl with good hydrodynamic performance, enabling efficient krill harvesting. Feng et al. [7] investigated the impacts of different structural parameters on the Antarctic krill trawl and provided optimization recommendations. Nsangué et al. [6] studied the effects of flow velocity, horizontal expansion ratio, sinker weight, buoyancy, and other factors on the performance of the Antarctic krill trawl. Currently, Antarctic krill harvesting is primarily carried out using two main types: the traditional otter trawl and the innovative continuous pump suction-type beam trawl (Figure 1) [8,9]. Norwegian fishing vessels utilizing the continuous pump suction-type beam trawl achieved an average annual catch per vessel that was more than three times higher than traditional single-ship otter trawl fishing vessels [10]. Under the total catch quota management system implemented in the Antarctic krill fishery [11], the continuous pump suction-type beam trawl shows promising and widespread applications.

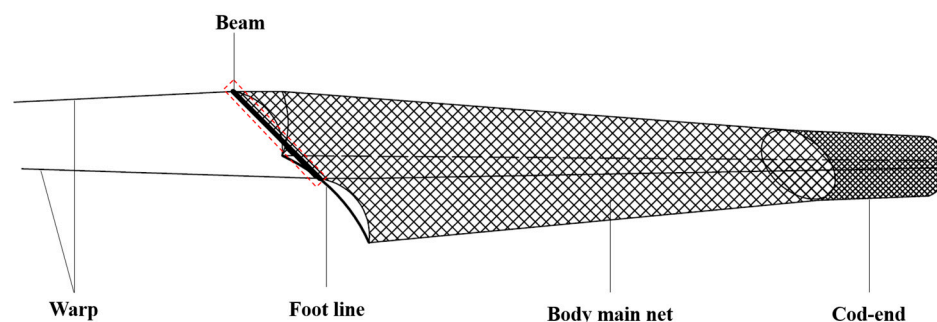


Figure 1. Schematic of the Antarctic beam trawl.

The continuous pump suction-type beam trawl utilizes a pump suction system installed at the end of the trawl net's cod-end. This system continuously transports the krill from the cod-end to storage holds on the ship through a conveying pipe, allowing for continuous underwater harvesting and production that can last for several days to weeks [12,13]. However, achieving high fishing efficiency with the continuous pump suction-type beam trawl in the Antarctic krill fishery depends on crucial factors, such as controlling the expansion of the trawl mouth during continuous harvesting and effectively adjusting the gear to the depth where the krill populations are located. This is because Antarctic krill exhibit irregular clustering and vertical movements, including diurnal vertical migration [14,15], which necessitates the careful control and adaptation of the gear during the harvesting process.

The headline of the beam trawl is fixed on the trawl beam, serving to uphold the horizontal expansion of the trawl. This ensures that the trawl's horizontal expansion remains stable, unaffected by the influence of waves and currents. Nevertheless, the hydrodynamic performance of the beam has a significant impact on the sinking performance, vertical expansion performance, and energy consumption of the fishing vessel. It is inconvenient to adjust the operating water layer of the fishing gear for the traditional beam trawl. However, by changing the shape of the beam, its hydrodynamics can be harnessed to provide lift

or sink forces to the trawl, achieving the purpose of adjusting the operating water layer. Therefore, it is necessary to conduct research on the hydrodynamic performance of the trawl beam.

The methods for the hydrodynamic performance of fishing gear and its components include offshore measurements, model experiments, and numerical simulations. Due to factors such as high costs, the time-consuming nature, and uncontrollable testing conditions, offshore measurements are significantly affected. Consequently, model experiments and numerical simulations are widely applied, due to their convenience and controllable testing conditions [16–19].

To investigate the hydrodynamic performances of different structural beams, the beam used on the “Shen Lan” krill trawler (Figure 2) served as the prototype. Three types of beams were designed: cylindrical, elliptical, and airfoil-shaped. Numerical simulations were employed to analyze the hydrodynamic performances of these three beams. Furthermore, the numerical simulation results were validated through model tests conducted in a circulating water tank. The results of this study are expected to serve as a theoretical foundation for the research and optimization design of the trawl beam’s hydrodynamic performance.



Figure 2. The Antarctic beam trawl used on the “Shen Lan” krill trawler.

2. Materials and Methods

2.1. Model of the Beam

The prototype of the beam (Figure 3) in this study is used in the “Shen Lan” Antarctic krill beam trawler, with a power of 8000 kW and an operation towing speed of 1.5 to 3.5 kn. The principal segment of the beam takes the form of a cylindrical structure, measuring 18 m in length (l_b) and 0.45 m in diameter (d_b). The beam is constructed from Q345 steel, with a wall thickness of 25 mm and weighing approximately 8 t. Semi-circular guides are symmetrically installed at both ends of the beam and the main section, being 1 m in length (l_g), 0.3 m in width (w_g), and 0.4 m in height (h_g).

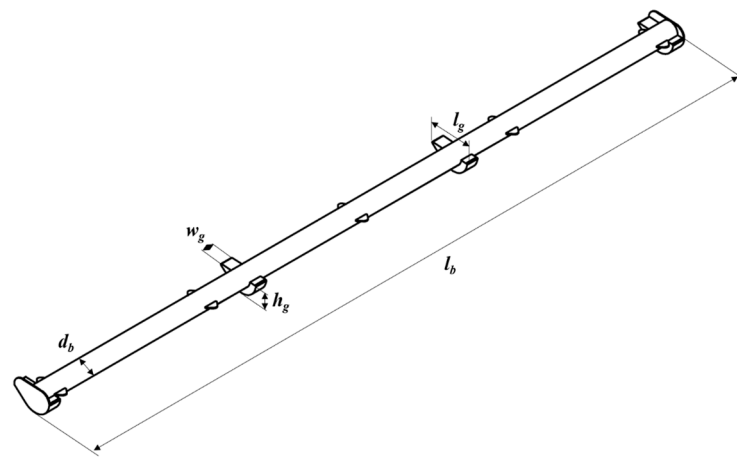


Figure 3. Schematic of the beam.

The model beam is designed based on the Froude criterion [20], and the conversion formular is as follows:

$$\frac{l_1}{l_2} = Fr \quad (1)$$

$$\frac{S_1}{S_2} = Fr^2 \quad (2)$$

$$\frac{v_1}{v_2} = \sqrt{Fr} \quad (3)$$

where 1 is the prototype, 2 is the model, l is the length, S is the plane area, v is the velocity, and Fr is the Froude number. According to the dimensions of the experimental flume tank, the Froude number in this study is 12.0.

To investigate the hydrodynamic performances of the beams with different shapes, the beams with airfoil and elliptical shapes are designed based on the prototype cylindrical beam (model 1). The three models maintain consistent chord lengths (c). The airfoil beam (model 2) employs the EPPLER 864 airfoil [21], characterized by a maximum thickness of 38.83% and a peak camber of 0.04%. Meanwhile, the elliptical beam (model 3) possesses a short axis length (height, h) identical to the maximum thickness (height, h) of the airfoil beam. The cross-sections of the three models are shown in Figure 4, and detailed parameters are outlined in Table 1.

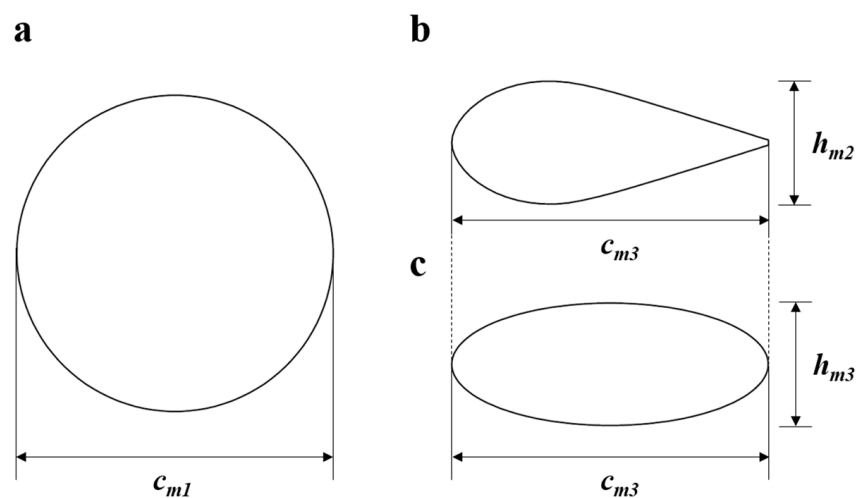


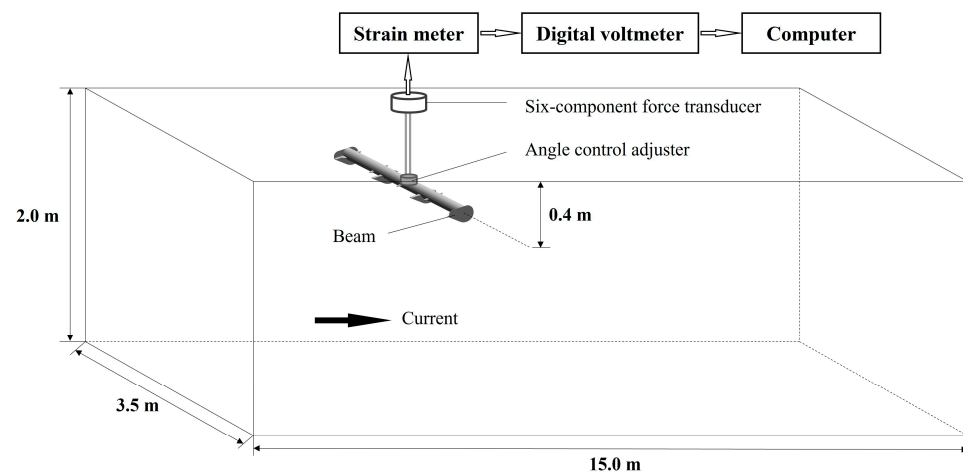
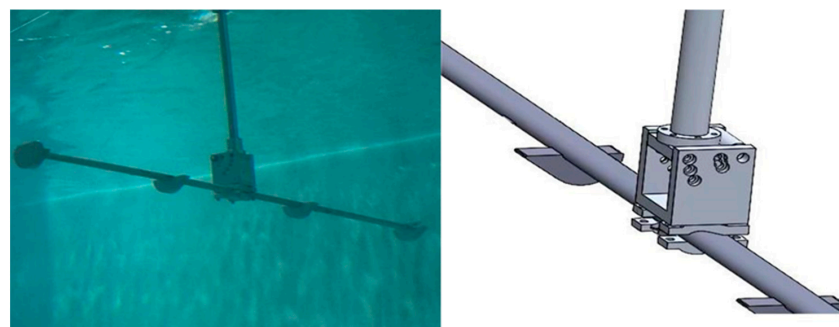
Figure 4. Cross-sections of the three beams. (a): Model 1, (b): model 2, (c): model 3.

Table 1. Parameters of the beams.

Parameters	Cross-Sectional Shape	Chord/mm	Length/mm	Height/mm	Plane Area/m ²
Prototype	Circular	450	18,000	450	8.100
Model 1	Circular	37.5	1500	37.5	0.056
Model 2	Airfoil	37.5	1500	14.6	0.056
Model 3	Ellipse	37.5	1500	14.6	0.056

2.2. Flume Test

The hydrodynamic assessments of the model beams were carried out in a circulation flume at Shanghai Ocean University, boasting dimensions of 15.0 m in length, 3.5 m in width, and a water depth of 2.0 m. The flow velocity of the flume spanned the spectrum from 0 to 1.5 m/s, meticulously governed with a precision of 1% in water velocity control. The observation section of the flume was 6.0 m in length and 3.3 m in width. The model beams were positioned 3.0 m downstream from the flow entrance and upheld at a distance of 0.4 m from the water surface (Figure 5). A six-component force transducer (0–200 N) was employed during the experiment to measure the lift force (F_L) and drag force (F_D) on the model beams. An angle control adjuster (Figure 6) was installed at the junction between the beam and the force transducer, which was used to adjust the angle of attack (AOA) of the beams during the experiment (Figure 7). The preliminary experiments on the bracket were conducted to measure the hydrodynamic force of the clamps and the angle control adjuster under different working conditions. The data in this paper were the final results after removing the influence of the bracket. The AOA was systematically varied within the range of -60° to 60° , with increments of 15° . The water temperature remained at approximately 20°C during the flume test.

**Figure 5.** Layout diagram of the flume test.**Figure 6.** Angle control adjuster.

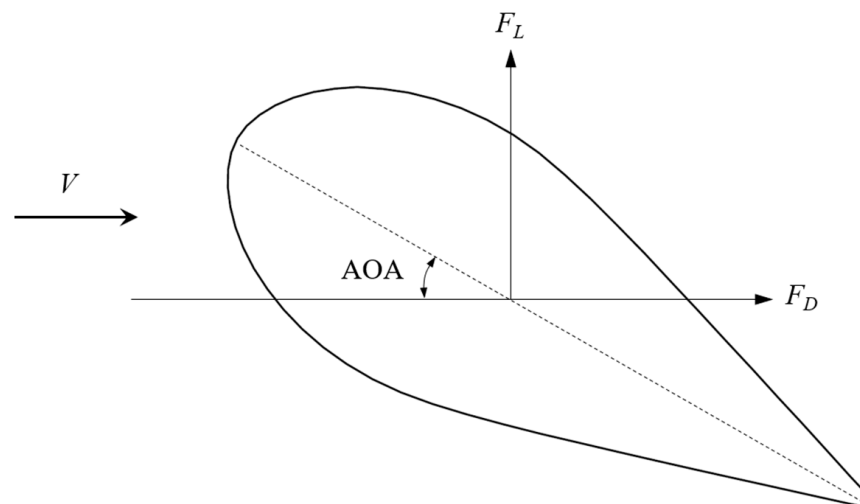


Figure 7. Parameter definition of the model beam.

2.3. Numerical Simulation

In the present study, the numerical simulation was carried out by the computational fluid dynamic (CFD) software CFX 18.2, which solved the steady Reynolds-averaged Navier–Stokes equations based on the framework of the element-based finite volume method [22]. The standard k - ϵ turbulence model combined with the explicit algebraic Reynolds stress model (EARSM) [23], an improved model from the typical standard k - ϵ model [24], was adapted to the simulation. Its precision was validated in prior investigations focused on the hydrodynamic characteristics of the rigid structures of the trawl [25–28]. The scalable wall treatment was employed for the wall function.

The computational domain, experimental arrangement, and setup for the CFD were of a comparable scale to the configurations that were examined in the flume tank experiments (Figure 5). The advection component of the velocity underwent spatial discretization using a high-resolution scheme within the CFX solver. In contrast, the treatment of turbulence-related factors, such as turbulent kinetic energy (k) and turbulent eddy dissipation (ϵ), was accomplished through the utilization of a 1st-order upwind scheme. The fluid was modeled as water, with a density (ρ) of 998.2 kg/m^3 and a viscosity (μ) of $1.003 \times 10^{-3} \text{ kg/(m}\cdot\text{s)}$. Further, the k and ϵ at the entrance of domain were calculated by following Xu et al. [29]. The current velocity was set at a uniform flow of 0.4 m/s (approximately 2.5 kn for the operation of full-scale trawls), of which the Reynolds number $Re = 1.50 \times 10^4$. Since the fluid could discharge completely, the pressure outlet was designated as the outlet boundary, with a relative pressure of 0 Pa . Smooth walls with non-slip conditions were used on the otter board surfaces, the side surfaces, and the bottom surface of the domain, while free slip walls were set on the other walls (Figure 8).

The unstructured tetrahedral grids were adopted in the far-field computational domain, and the near-wall region was refined with the 8-layer prismatic layers (Figure 9). The first layer thickness was $2.0 \times 10^{-4} \text{ m}$ to ensure $y^+ \geq 15$. Hence, the wall function was employed to handle near-wall interactions within the high- Re separation flow. Additionally, a mesh convergence test was executed to validate the accuracy of the numerical simulation, of which drag and lift force were selected as the target indices. As shown in Figure 10, both the lift coefficient and drag coefficient achieved stability when the grid count reached 2 million. The deviations of the drag and lift forces among the last three cases were less than 1%. Considering the balance of computational efficiency and accuracy, the total number of elements and nodes totaled approximately 2.52×10^6 and 5.17×10^5 , respectively.

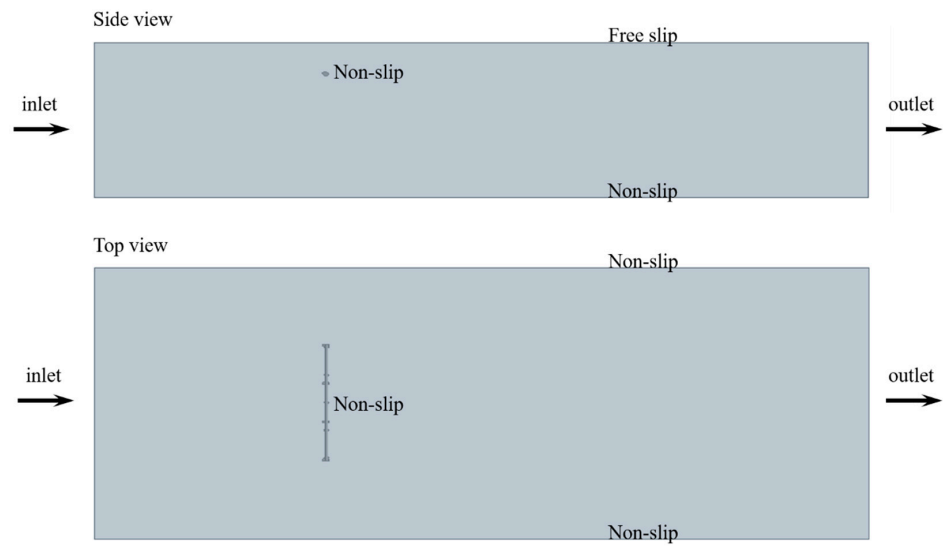


Figure 8. Boundary conditions of the computational domain.

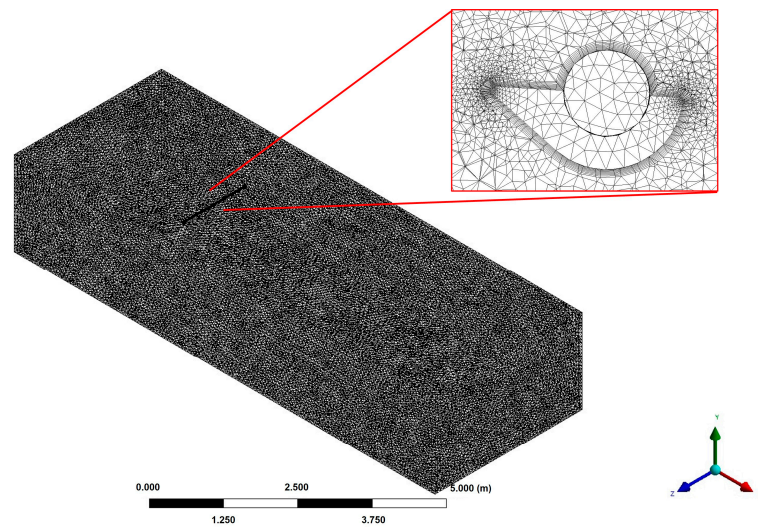


Figure 9. Grid generation in the computational domain.

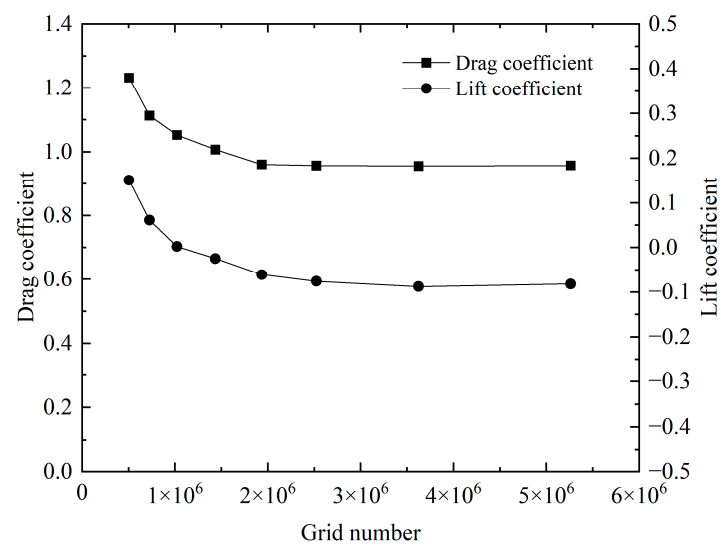


Figure 10. Grid independence test.

2.4. Data Process

The lift force F_L and drag force F_D of the beams were measured in the flume tank test and numerical simulation. The lift coefficient C_L , drag coefficient C_D , lift-to-drag ratio K , and Reynolds number Re were calculated after the strut interference correction. The calculation formulae are as follows:

$$C_L = \frac{2F_L}{\rho S u^2} \quad (4)$$

$$C_D = \frac{2F_D}{\rho S u^2} \quad (5)$$

$$Re = \frac{u c}{\mu} \quad (6)$$

$$K = \frac{C_L}{C_D} \quad (7)$$

where ρ is the fluid density; S is the area of the beam model; u is the flow velocity; c is the chord length of the beam; and μ is the dynamic viscosity coefficient of fluid.

3. Results

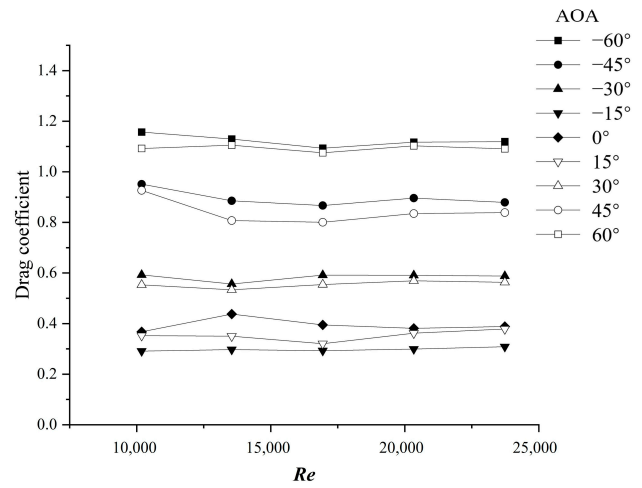
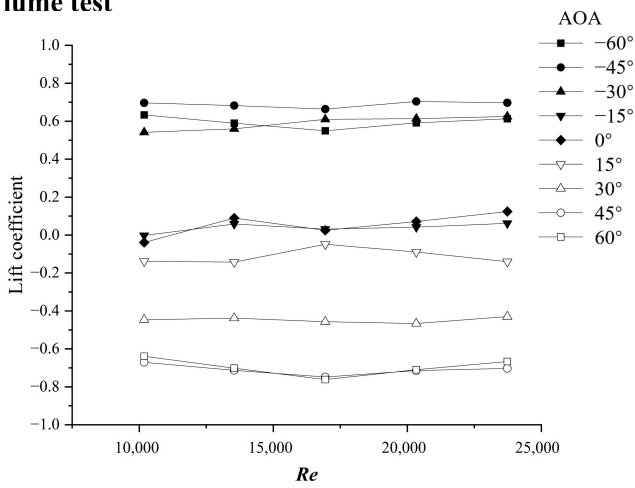
3.1. Validation

In order to verify the accuracy of the numerical simulation method selected in this study, a comparative study was conducted between the flume test and numerical simulations on the airfoil and cylindrical beams. The relationship between hydrodynamic coefficients (C_L , C_D) of the airfoil beam (model 2) and Re for each AOA are depicted in Figure 11. As shown in the figures, the C_L and C_D for the beam exhibited a tendency to stabilize when the flow velocity exceeded 0.36 m/s ($Re > 1.35 \times 10^5$), and it was in the critical Re region [30] or the so-called self-modeling region [27]. Therefore, the C_L and C_D of the beams are discussed in the following sections with the flow velocity of 0.4 m/s ($Re = 1.50 \times 10^4$).

The C_L and C_D for the airfoil beam and cylindrical beam are presented in Figures 12 and 13, reflecting data from the flume test and numerical simulation. The numerical simulation results exhibited a consistent trend when compared with the results from the flume test.

For the cylindrical beam, the C_D remained between 0.954 and 1.084 (based on the flume test) and between 0.825 and 1.043 (based on numerical simulation) for AOAs ranging from -60° to 60° . Overall, there was a tendency for the C_D to increase with the increasing absolute value of the AOA. Results from both the flume test and the numerical simulation showed that for the AOA less than 0° , the C_D of the beam increased from 0.854 to 1.084 and from 0.925 to 1.036 as the absolute value of the AOA increased, respectively. For the AOA greater than 0° , the C_D increased with the increasing AOA and reached its maximum value at an AOA of 45° , being 1.063 and 0.043, respectively. For the AOA greater than 45° , the C_D of the beam started to decrease. The numerical simulation results can accurately simulate the values and trends of the drag coefficient of the cylindrical beam, with an average error of 3.24%. The C_L remained between -0.056 and 0.032 (based on flume test) and between -0.087 and 0.075 (based on numerical simulation) for AOAs ranging from -60° to 60° . The C_L of the beam showed no significant correlation with the AOA (flume test: $p = 0.43$, numerical simulation: $p = 0.42$).

Flume test



Numerical simulation

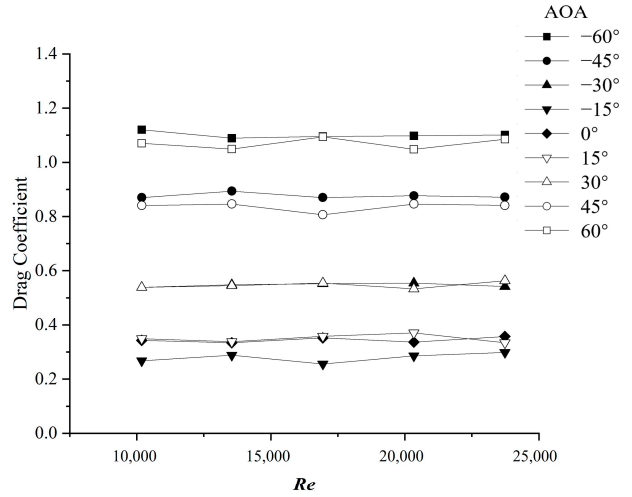
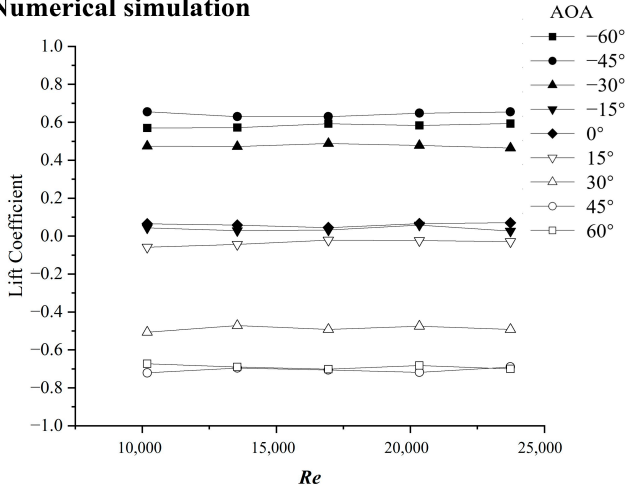


Figure 11. Relationship between hydrodynamic coefficients and the Reynolds number.

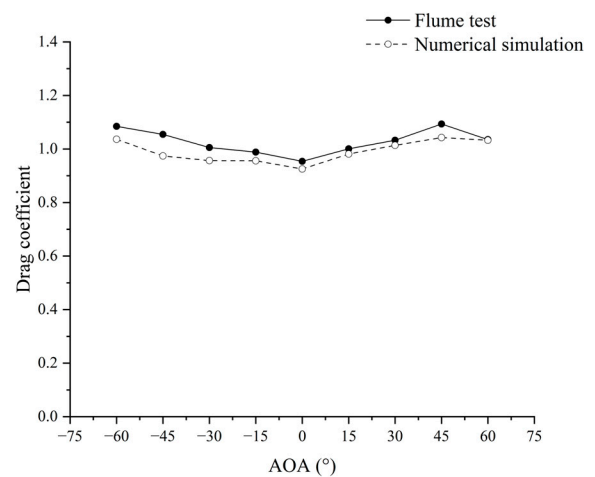
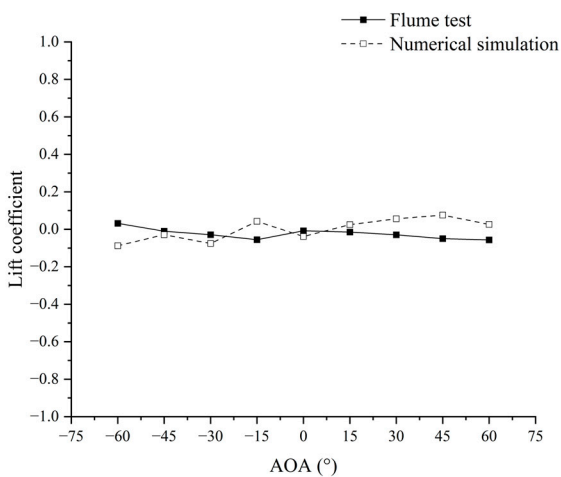


Figure 12. Relationship between hydrodynamic coefficients of the cylindrical beam and angles of attack.

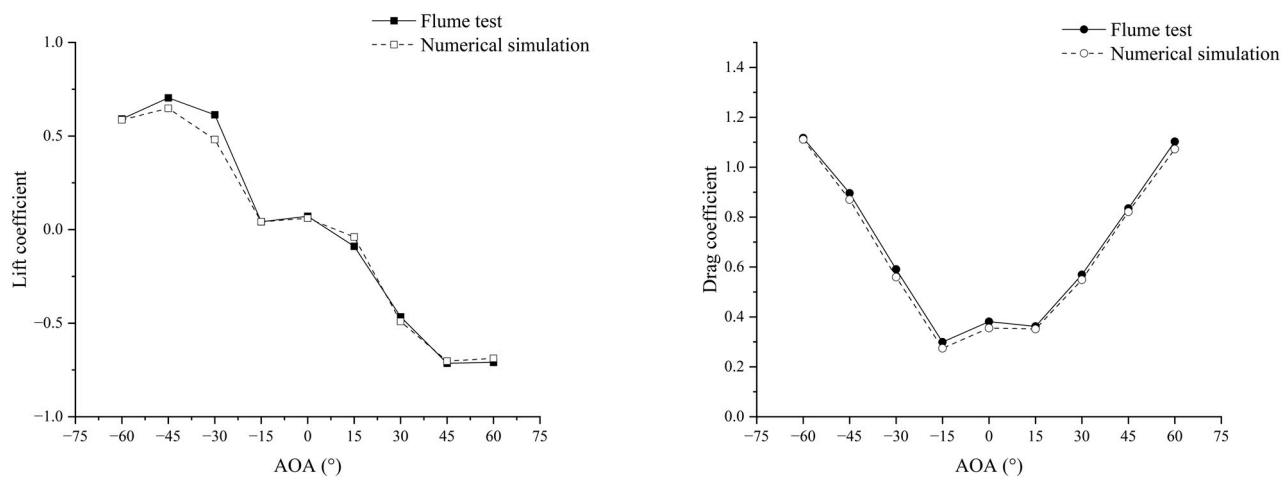


Figure 13. Relationship between hydrodynamic coefficients of the airfoil beam and angles of attack.

For the airfoil beam, the relationship between the C_D and the AOA demonstrated axisymmetric distribution around $AOA = 0^\circ$. The C_D initially decreased and then increased as the absolute value of AOA increased. When the AOA was negative, both flume tests and numerical simulations showed that the C_D reached the minimum value at an AOA of -15° , with values of 0.299 and 0.274, respectively. Subsequently, the C_D increased with the increase in the absolute value of the AOA. For positive AOAs, the C_D of the beam reached its minimum value at an AOA of 15° , with values of 0.362 (flume test) and 0.351 (numerical simulation), and then increased as the angle of attack further increased. The C_L versus AOA relationship for the airfoil beam exhibited central symmetry at about $AOA = 0^\circ$. Both flume tests and numerical simulations revealed that within the angle of attack range of -60° to 60° , the C_L of the beam initially increased with the increasing AOA. Specifically, the C_L reached its maximum values of 0.704 and 0.648 at an AOA of -45° , respectively. Subsequently, as the AOA continued to increase, the C_L gradually decreased, reaching its minimum values of -0.714 and -0.703 at an AOA of 45° . For the AOA greater than 45° , the C_L increased as the AOA further increased. It is worth noting that the simulation results for C_D and C_L are slightly smaller than those obtained from the flume test. The average errors between the numerical simulation and flume test are 3.86% for C_D and 11.04% for C_L .

In summary, for the hydrodynamic performance study of beams with different shapes, the numerical simulation results align closely with the flume test results, exhibiting similar trends and accurately reflecting the critical angle of attack. Therefore, the numerical simulation method chosen in this study is deemed suitable for investigating the hydrodynamic performance of the beam for the trawl.

3.2. The Relationship between the Hydrodynamic Coefficients of Beams and the Angles of Attack

Based on the results presented earlier, the CFD approach using the $k-\varepsilon$ EARS model is suitable for studying the hydrodynamic performance of beams using an in-trawl net. In this section, the numerical method was utilized to investigate the hydrodynamic performance of the beams.

The relationship between the hydrodynamic coefficients of beams with different shapes and the angles of attack are depicted in Figure 14 (Model 1: cylindrical beam, Model 2: airfoil beam, and Model 3: elliptical beam). Overall, the C_D of the beams exhibited an increasing trend with the absolute value of the increasing AOA. However, the variation in AOA has minimal impact on the C_D of the cylindrical beam. The cylindrical beam's drag coefficient was on average 49.54% higher than that of the airfoil beam and 59.74% higher than that of the elliptical beam. The trend in drag coefficient changes for the elliptical beam resembled that of the airfoil beam. As the absolute value of the AOA increased, the C_D of the elliptical and airfoil beams reached their respective maximum values of 1.098 and 1.111 at AOAs of 60° and -60° , similar to the C_D of the cylindrical beam. Notably, the C_D of the

airfoil beam reached its minimum value of 0.274 at an AOA of -15° , while the C_D of the elliptical beam reached its minimum value of 0.167 at an AOA of 0° . For an AOA less than 0° , the C_D of the elliptical beam was slightly lower than that of the airfoil beam, while for angles greater than 0° , the C_D of the elliptical beam was slightly higher than that of the airfoil beam.

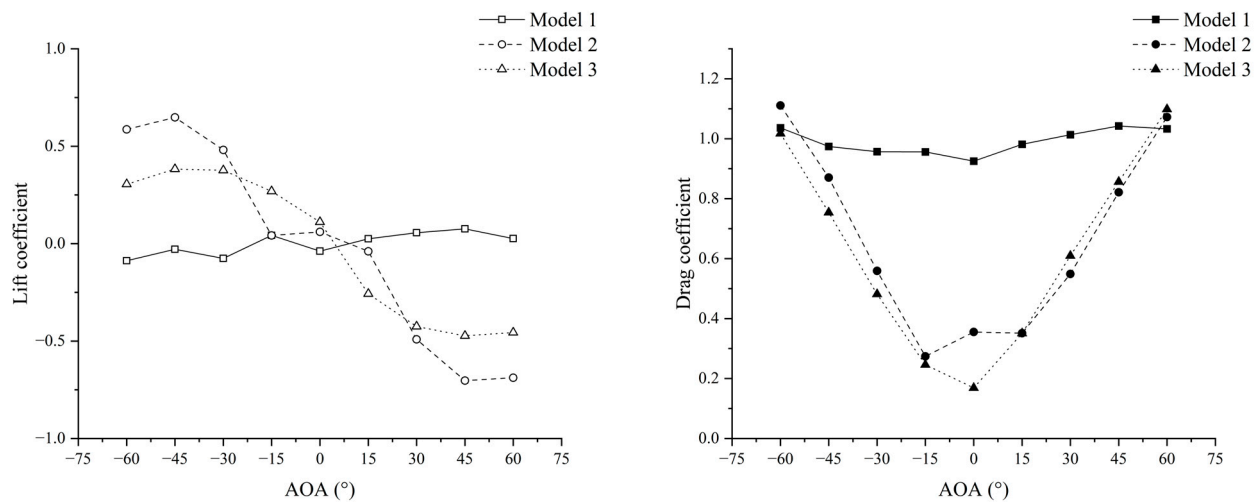


Figure 14. Relationship between hydrodynamic coefficients of beams and angles of attack.

Regarding the lift coefficient, as previously mentioned, there was no significant relationship between the C_L and the AOA for the cylindrical beam, and the lift coefficient was 87.79% lower than that of the airfoil beam and 85.06% lower than that of the elliptical beam on average, respectively. However, for angles of attack with an absolute value greater than 15° , both the airfoil and elliptical beams exhibited significantly higher C_L , compared to the cylindrical beam. The relationship between the C_L and the AOA for the elliptical beam was similar to that of the airfoil beam, showing an initial increase followed by a decrease with increasing AOA. When the AOA was greater than 0° , the minimum C_L for the airfoil and elliptical beams occurred at an AOA of 45° , with values of -0.703 and -0.473 , respectively, representing a difference of 48.63%. Conversely, for an AOA less than 0° , the maximum lift coefficient for the airfoil beam occurred at an AOA of -45° , with a value of 0.648, which is 69.19% higher than the maximum C_L for the elliptical beam. For larger AOAs ($|\text{AOA}| \geq 30^\circ$), the average C_L of the airfoil beam was 50.69% greater than that of the elliptical beam. However, for $|\text{AOA}| \leq 15^\circ$, the lift coefficient of the elliptical beam was greater.

3.3. The Relationship between the Lift-to-Drag Ratio of Beams and the Angles of Attack

The lift-to-drag ratio (K) serves as a valuable metric for assessing the aerodynamic [31] or hydrodynamic performance of objects immersed in a fluid. It characterizes the efficiency of these objects under specific conditions. Furthermore, the lift-to-drag ratio plays a pivotal role in the hydrodynamic research of components for trawls, such as otter boards [28,29,32,33]. In this study, the lift-to-drag ratios for beams are shown in Figure 15.

For the cylindrical beam, the correlation between K and AOA was relatively insignificant. Over an AOA range of -60° to 60° , the lift-to-drag ratio of cylindrical beams only fluctuated between -0.085 and 0.079 . In contrast, the absolute values of the lift-to-drag ratios for airfoil and elliptical beams exhibited a trend of initially increasing and then decreasing with the increasing absolute value of the angle of attack. The lift-to-drag ratio for the airfoil beam reached its maximum values of 0.861 and -0.894 at AOAs of -30° and 30° , respectively, while for the elliptical beam, it reached its maximum value of 1.092 and its minimum value of -0.733 at angles of attack of -15° and 15° , respectively. Therefore, it

can be observed that both the airfoil and elliptical beams exhibited enhanced efficiency at lower angles of attack.

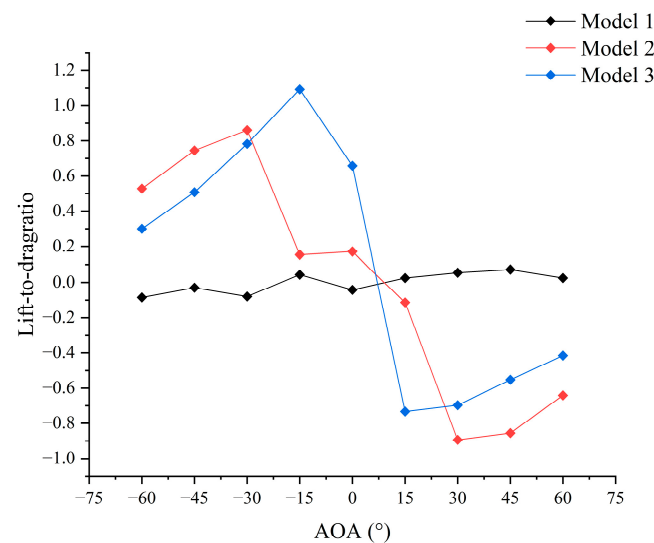


Figure 15. Relationship between lift-to-drag ratios of beams and angles of attack.

4. Discussion

4.1. Influence of Shape on the Hydrodynamic Performance of the Beam

The beam trawl is a type of midwater trawl that employs targeted fishing methods. During operation, quickly adjusting the trawl to the appropriate water depth is beneficial for the precise targeting of the catch, thereby enhancing the efficiency of the trawl [34]. Based on the findings of this study, when comparing the three beams, airfoil and elliptical beams offered a certain lift and dive potential to the beam at different angles of attack. This allows for the adjustment of the angle of attack during operation to achieve the rise and descent of the beam and trawl, thereby facilitating the rapid adjustment of the water depth. In contrast, the cylindrical beam showed less noticeable changes in the lift-to-drag coefficient at different angles of attack. For airfoil and elliptical beams, their drag coefficient values and variation trends are generally consistent (relative mean deviation (RMD) = 7.97%), except at a 0° AOA. At higher angles of attack ($|\text{AOA}| \geq 30^\circ$), the lift coefficient of the airfoil beam is greater than that of the elliptical beam. However, the lift coefficient of the elliptical beam is more stable (RMD of the elliptical beam is 6.61%, and RMD of the airfoil beam is 12.53%) under these angles of attack.

When it comes to practical production operations, it is essential to consider not only the hydrodynamic performance of the beam but also factors such as beam production costs and the actual operating conditions of the trawl. Compared to the airfoil beam, the elliptical beam has a symmetrical structure, making its production simpler and more cost-effective while ensuring a more stable hydrodynamic performance. This makes the beam better suited for use in fisheries production. Furthermore, during actual operations, the angle of attack for the beam is relatively small. According to the research results, the elliptical beam exhibited a higher lift coefficient at small angles of attack, providing greater lift. Therefore, it is worth considering the use of the elliptical beam for beam trawl net operations.

4.2. Flow Distribution around the Beams

Flow field visualization is a method to visually display changes in the flow field around the component, providing a theoretical foundation for the analysis and optimization design of beam hydrodynamic performance. Flow field visualization methods encompass hydrogen bubble simulation, particle image velocimetry, streamline visualization, and numerical simulation, among others [35,36]. The numerical simulation method was employed to

conduct a visualization study of the flow distribution around the beams. The streamlines and velocity vector at the cross-section of the beams are shown in Figure 16.

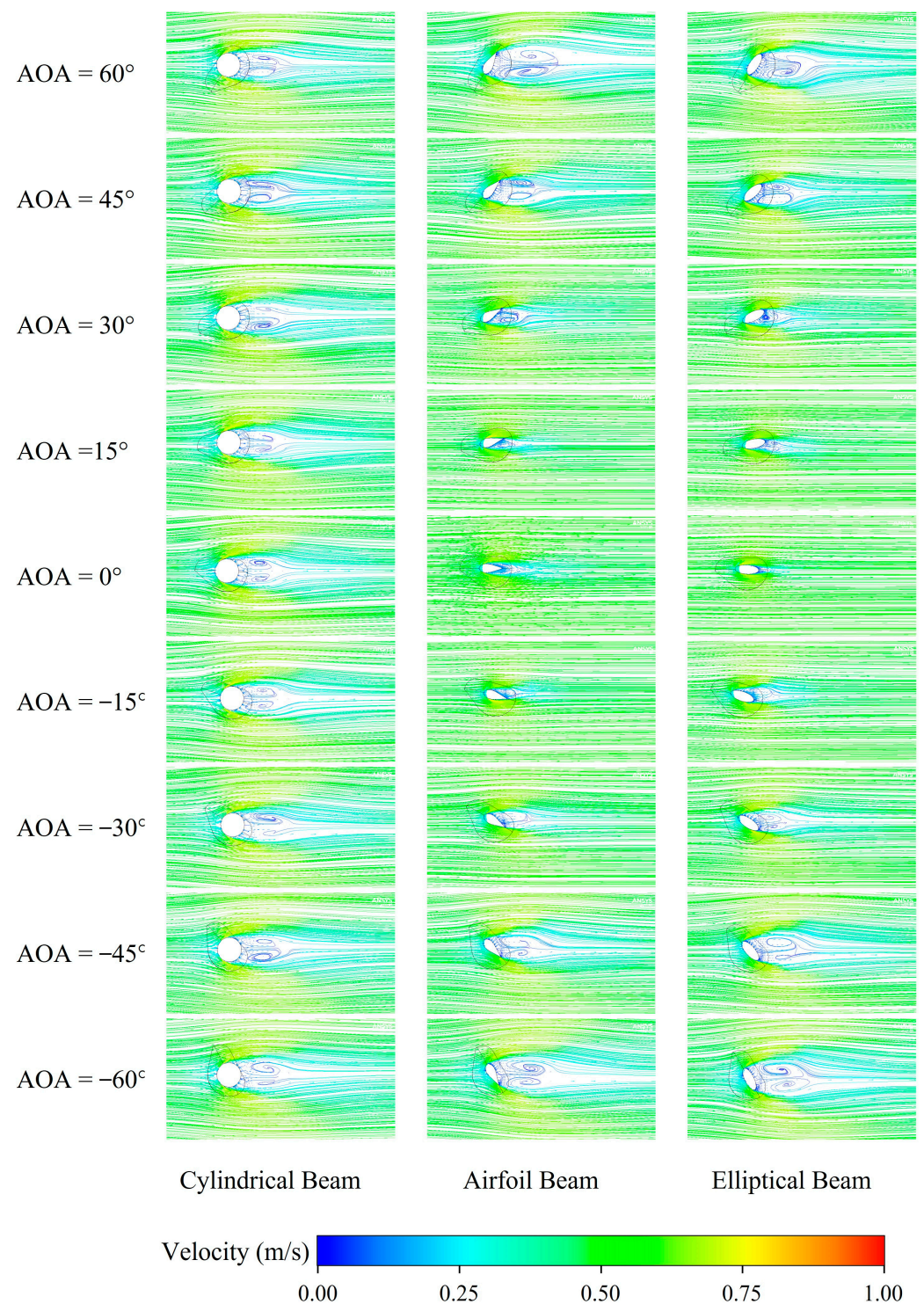


Figure 16. Streamlines and velocity vector at the cross-section of the beams.

At various angles of attack, there are two symmetric vortices behind the cylindrical beam, and the vortices do not develop or disappear with changes in the angle of attack. This explains why the lift coefficient and drag coefficient of the cylindrical beam do not change significantly at different AOAs. In contrast to the flow field around the cylindrical beam, at smaller angles of attack, neither the airfoil beam nor the elliptical beam generates

vortices behind them. However, as the angle of attack increases, vortices begin to form and develop behind the beams' back surfaces. Along with this development, the separation points of the flow continuously shift. With further increases in the angle of attack, the vortices grow larger and gradually cover the back surfaces of the beams.

For the airfoil beam and elliptical beam, at an angle of attack of 0° , the low-velocity area ($u < 0.2$ m/s) behind the airfoil beam is significantly larger than that behind the elliptical beam. At this angle of attack, the pressure difference before and after the airfoil beam is 233 Pa, while for the elliptical beam, it is 191 Pa. Therefore, at this angle of attack, the airfoil beam has a higher drag coefficient. As the angle of attack continuously increases, vortices start forming on the leeward surface of the beams, and flow separation begins to occur on the beam's surface, gradually moving forward. From the streamlines, it can be observed that at an angle of attack of 45° (-45°), the flow separation point moves forward to the very front, and vortices also begin to shed. Therefore, in this study, 45° can be considered the critical angle of attack for both the airfoil and elliptical beams, where the beam's lift coefficient is at its maximum. At angles of attack greater than 45° , the lift coefficient of the beams starts to decrease.

5. Conclusions

The hydrodynamic performance of the beam used in the Antarctic krill beam trawl was studied in the present work. A model test in a flume tank was carried out to validate the accuracy of the CFD method, and the results showed good agreement. Three different shapes of beams were designed based on the beam used by the "Shen Lan" trawler. The hydrodynamic characteristics of beams with different shapes were studied using numerical simulation, and the flow field distribution around the beams was analyzed. The following conclusions were drawn from the work:

- The CFD method chosen in this study can relatively accurately predict the values and trends of the hydrodynamic coefficients of the beam with changing angles of attack, making it suitable for researching the hydrodynamic performance of the beam.
- Changes in the angle of attack significantly affect the hydrodynamic coefficients of the airfoil beam and the elliptical beam but have a minor impact on the cylindrical beam.
- As the angle of attack increases, the lift coefficient of the airfoil beams surpasses that of the elliptical beam, while at smaller angles of attack, the elliptical beam exhibits a higher lift coefficient.
- At an angle of attack of 45° , the absolute values of the lift coefficients for the airfoil beam and the elliptical beam reach their maximum values, which are 0.703 and 0.473, respectively.

The differences in the hydrodynamic performances of beams with different shapes were studied in this study. Compared with traditional trawls that use sinkers and floats to adjust the operating water depth, it is more convenient and more maneuverable to change the shape and angle of attack of the beams to obtain hydrodynamic force and provide sinking force and buoyancy for the trawl. The research results of this paper can provide a reference for further obtaining truss structures with better hydrodynamic performance and establishing a water depth adjustment mechanism for beam trawl operations.

In a deeper view, optimizing the structural parameters of the beams, including aspects such as aspect ratio, thickness, curvature, etc., based on the actual conditions of the vessel and trawl will be essential to obtain the optimal structural parameters for the beams. Subsequently, the impacts of these optimally designed beams on enhancing efficiency and reducing costs in fishing operations will be assessed. Furthermore, it is necessary to carry out research on the matching of beams, trawls, and fishing vessels. In addition, high-fidelity CFD methods can be employed to further analyze the flow separation or turbulent energies of beams, thereby enriching the research conclusions regarding beam hydrodynamics.

Author Contributions: Conceptualization, Y.L., X.Z. and Y.W.; methodology, Y.L. and Y.W.; software, Y.L. and Z.L.; validation, Y.L., Z.W. and S.M.; formal analysis, Y.L. and Z.L.; investigation, Y.L., Z.L. and G.Q.; resources, X.Z., Y.Z. and L.W.; data curation, Y.L., Z.L. and Y.W.; writing—original draft preparation, Y.L.; writing—review and editing, Y.L., Z.L., Z.W., X.Z. and Y.W.; visualization, Y.L.; supervision, X.Z. and Y.W.; project administration, X.Z. and L.W.; funding acquisition, Y.W. and Z.W. All authors have read and agreed to the published version of the manuscript.

Funding: This research was funded by the National Natural Science Foundation of China (32002444) and the Shanghai Sailing Program (23YF1459700).

Data Availability Statement: Data are unavailable due to privacy restrictions.

Acknowledgments: We would like to thank the College of Marine Science at Shanghai Ocean University for the support they provided for the flume test in this study.

Conflicts of Interest: The authors declare no conflicts of interest.

References

- Nicol, S.; Foster, J.; Kawaguchi, S. The fishery for Antarctic krill—Recent developments. *Fish Fish.* **2012**, *13*, 30–40. [[CrossRef](#)]
- Wan, R.; Jia, M.; Guan, Q.; Huang, L.; Cheng, H.; Zhao, F.; He, P.; Hu, F. Hydrodynamic performance of a newly-designed Antarctic krill trawl using numerical simulation and physical modeling methods. *Ocean Eng.* **2019**, *179*, 173–179. [[CrossRef](#)]
- Costanzo, M.; Cesi, V.; Prete, E.; Negroni, A.; Palone, F.; Cucchiara, S.; Oliva, S.; Leter, B.; Stronati, L. Krill oil reduces intestinal inflammation by improving epithelial integrity and impairing adherent-invasive *Escherichia coli* pathogenicity. *Dig. Liver Dis.* **2016**, *48*, 34–42. [[CrossRef](#)] [[PubMed](#)]
- Tang, H.; Nsangué, B.T.N.; Pandong, A.N.; He, P.; Liuxiong, X.; Hu, F. Flume tank evaluation on the effect of liners on the physical performance of the Antarctic krill trawl. *Front. Mar. Sci.* **2022**, *8*, 829615. [[CrossRef](#)]
- Nicol, S.; Jacqueline, F. *Biology and Ecology of Antarctic Krill*; Springer International Publishing: Berlin/Heidelberg, Germany, 2016; pp. 387–421.
- Nsangué, B.T.N.; Tang, H.; Pandong, A.N.; Xu, L.; Adekunle, D.M.; Hu, F. Examining engineering performance of midwater trawl with different horizontal spread ratio, floatage, and weight parameters: A case study of model net for Antarctic krill fisheries. *Int. J. Nav. Archit. Ocean Eng.* **2022**, *14*, 100448. [[CrossRef](#)]
- Feng, C.; Liu, J.; Zhang, Y.; Zhang, X.; Zhou, A.; Wang, L. Structure improvement design and performance experiment of Antarctic krill trawl net. *Trans. Chin. Soc. Agric. Eng.* **2017**, *33*, 75–81. [[CrossRef](#)]
- Krafft, B.A.; Krag, L.A. Assessment of mortality of Antarctic krill (*Euphausia superba*) escaping from a trawl. *Fish. Res.* **2015**, *170*, 102–105. [[CrossRef](#)]
- He, R.; Zheng, H.; Ma, S.; Wu, Y.; Yang, S.; Dai, Y.; Wang, Y. Hydrodynamic simulation and experiment of depth adjustable beam trawl for Antarctic krill. *J. Mar. Sci. Technol.* **2023**, *28*, 399–409. [[CrossRef](#)]
- CCAMLR. *Statistical Bulletin*; CCAMLR: Hobart, Australia, 2021; Volume 33.
- CCAMLR. *Report of the Twenty-Eighth Meeting of the Commission*; CCAMLR: Hobart, Australia, 2009; No. CCAMLR-XXVIII.
- Summerfelt, S.T.; Davidson, J.; Wilson, G.; Waldrop, T. Advances in fish harvest technologies for circular tanks. *Aquac. Eng.* **2009**, *40*, 62–71. [[CrossRef](#)]
- Liu, J.; Huang, H.L.; Li, L.Z.; Chen, S.; Wu, Y.; Xu, G.; Xu, B. Research progress of Antarctic krill (*Euphausia superba*) continuous fishing techniques. *Fish. Mod.* **2013**, *40*, 51–54. (In Chinese) [[CrossRef](#)]
- Zhu, G.P.; Wei, L. Age and growth of Antarctic fish species: A review. *J. Fish. China* **2017**, *41*, 1638–1647. (In Chinese) [[CrossRef](#)]
- Huang, H.L.; Chen, X.Z.; Feng, C.L. Analysis of the current situation of Antarctic krill resource development. *Fishery Mod.* **2007**, *1*, 48–51. (In Chinese)
- Mellibovsky, F.; Prat, J.; Notti, E.; Sala, A. Otter board hydrodynamic performance testing in flume tank and wind tunnel facilities. *Ocean Eng.* **2018**, *149*, 238–244. [[CrossRef](#)]
- Bi, C.W.; Zhao, Y.P.; Dong, G.H.; Xu, T.-J.; Gui, F.-K. Numerical simulation of the interaction between flow and flexible nets. *J. Fluids Struct.* **2014**, *45*, 180–201. [[CrossRef](#)]
- Huang, L.Y.; Li, Y.Y.; Wang, G.; Wang, Y.; Wu, Q.; Jia, M.; Wan, R. An improved Morison hydrodynamics model for knotless nets based on CFD and metamodelling methods. *Aquac. Eng.* **2022**, *96*, 102220. [[CrossRef](#)]
- Guan, Q.L.; Zhu, W.B.; Zhou, A.Z.; Wang, Y.; Tang, W.; Wan, R. Numerical and Experimental Investigations on Hydrodynamic Performance of a Newly Designed Deep Bottom Trawl. *Front. Mar. Sci.* **2022**, *9*, 891046. [[CrossRef](#)]
- Ashton, G.D. Froude Criterion for Ice-Block Stability. *J. Glaciol.* **1974**, *13*, 307–313. [[CrossRef](#)]
- Chemezov, D.; Balabanov, P.; Polyakov, K.; Kornev, N.; Toloake, D.; Dokuchaev, I.; Zharkov, I. Reference data of pressure distribution on the surfaces of airfoils (hydrofoils) having the names beginning with the letter E (the second part). *ISJ Theor. Appl. Sci.* **2022**, *1*, 601–671. [[CrossRef](#)]
- Filippini, G.; Maliska, C.R.; Vaz, M. A physical perspective of the element-based finite volume method and FEM-Galerkin methods within the framework of the space of finite elements. *Int. J. Numer. Methods Eng.* **2014**, *98*, 24–43. [[CrossRef](#)]

23. Wallin, S.; Johansson, A.V. Modelling streamline curvature effects in explicit algebraic Reynolds stress turbulence models. *Int. J. Heat Fluid Flow* **2002**, *23*, 721–730. [[CrossRef](#)]
24. Shih, T.H.; Liou, W.W.; Shabbir, A.; Yang, Z.; Zhu, J. A new k- ϵ eddy viscosity model for high Reynolds number turbulent flows. *Comput. Fluids* **1995**, *24*, 227–238. [[CrossRef](#)]
25. Xu, Q.C.; Feng, C.L.; Huang, L.Y.; Xu, J.Q.; Wang, L.; Zhang, X.; Liang, Z.L.; Tang, Y.L.; Zhao, F.F.; Wang, X.X.; et al. Parameter optimization of a double-deflector rectangular cambered otter board: Numerical simulation study. *Ocean Eng.* **2018**, *162*, 108–116. [[CrossRef](#)]
26. Wang, G.; Huang, L.Y.; Wang, L.; Zhao, F.; Li, Y.; Wan, R. A metamodeling with CFD method for hydrodynamic optimisations of deflectors on a multi-wing trawl door. *Ocean Eng.* **2021**, *232*, 109045. [[CrossRef](#)]
27. Li, Y.Y.; Huang, L.Y.; Wang, G.; Xu, Q.; Jia, M. Study of the Structural Effects on the Hydrodynamics of a Hollow Rectangular Cambered Otter Board Using the CFD Method. *Int. J. Offshore Polar Eng.* **2022**, *32*, 348–355. [[CrossRef](#)]
28. Li, Y.Y.; Wang, G.; Xu, Q.C.; Wang, X.; Zhang, R.; Huang, L. Study of the Influence of Aspect Ratios on Hydrodynamic Performance of a Symmetrical Elliptic Otter Board. *Symmetry* **2022**, *14*, 1566. [[CrossRef](#)]
29. Xu, Q.C.; Huang, L.Y.; Li, X.S.; Li, Y.; Zhao, X. Parameter optimization of a rectangular cambered otter board using response surface method. *Ocean Eng.* **2020**, *220*, 108475. [[CrossRef](#)]
30. Pope, S. *Turbulent Flows*; Cambridge University Press: Cambridge, UK, 2000. [[CrossRef](#)]
31. Anderson, J.D. *Fundamentals of Aerodynamics*; McGraw Hill Higher Education: Chicago, IL, USA, 2011.
32. You, X.X.; Hu, F.X.; Zhuang, X.; Dong, S.; Shiode, D. Effect of wingtip flow on hydrodynamic characteristics of cambered otter board. *Ocean Eng.* **2021**, *222*, 108611. [[CrossRef](#)]
33. Wang, L.; Zhang, X.; Wan, R.; Xu, Q.; Qi, G. Optimization of the Hydrodynamic Performance of a Double-Vane Otter Board Based on Orthogonal Experiments. *J. Mar. Sci. Eng.* **2022**, *10*, 1177. [[CrossRef](#)]
34. Hu, F.; Matuda, K.; Sato, K. Characteristics of Dynamic Control of Midwater Trawl System in Field Experiments. *Nippon. Suisan Gakkaishi* **1994**, *60*, 493–497. [[CrossRef](#)]
35. Takahashi, Y.; Fujimori, Y.; Hu, F.; Shen, X.; Kimura, N. Design of trawl otter boards using computational fluid dynamics. *Fish. Res.* **2015**, *161*, 400–407. [[CrossRef](#)]
36. You, X.X.; Hu, F.X.; Dong, S.C.; Takahashi, Y.; Shiode, D. Shape optimization approach for cambered otter board using neural network and multi-objective genetic algorithm. *Appl. Ocean Res.* **2020**, *100*, 102148. [[CrossRef](#)]

Disclaimer/Publisher’s Note: The statements, opinions and data contained in all publications are solely those of the individual author(s) and contributor(s) and not of MDPI and/or the editor(s). MDPI and/or the editor(s) disclaim responsibility for any injury to people or property resulting from any ideas, methods, instructions or products referred to in the content.